arXiv:1410.0851v2 [nucl-th] 19 Oct 2014

Effects of the symmetry energy on properties of neutron star crusts near the neutron drip density

S. S. Bao, J. N. Hu, Z. W. Zhang, and H. Shen*

School of Physics, Nankai University, Tianjin 300071, China

Abstract

We study the effects of the symmetry energy on the neutron drip density and properties of nuclei in neutron star crusts. The nonuniform matter around the neutron drip point is calculated by using the Thomas–Fermi approximation with the relativistic mean-field model. The neutron drip density and the composition of the crust are found to be correlated with the symmetry energy and its slope. We compare the self-consistent Thomas–Fermi approximation with other treatments of surface and Coulomb energies, and find that these finite-size effects play an essential role in determining the equilibrium state at low density.

PACS numbers: 26.60.-c, 26.60.Gj, 21.65.Cd

Keywords: Symmetry energy, Neutron drip density, Thomas–Fermi approximation

*Electronic address: shennankai@gmail.com

I. INTRODUCTION

Neutron star crusts are important laboratories for the study of asymmetric nuclear matter at subnuclear density [1–3]. The crust is divided into an outer crust and an inner crust at the neutron drip density $n_{\rm drip} \sim 4 \times 10^{11}\,{\rm g\,cm^{-3}}$ where neutrons begin to drip out of nuclei [4]. It is well known that the outer crust consists of a lattice of nuclei with a gas of electrons, while the inner crust contains neutron-rich nuclei, dripped neutrons, and relativistic electrons [1–3]. Great efforts have been devoted to the study of neutron star crusts because of their importance in astrophysical observations and complex phase structure [1–8]. At low densities around $n_{\rm drip}$, the stable shape of the nucleus is spherical, but it may change from droplet to rod, slab, tube, and bubble, known as nuclear pasta phases, at relatively high densities [9–12]. The neutron drip density is determined by the neutron chemical potential, which is strongly dependent on the nuclear symmetry energy and its density dependence. Therefore, it is interesting to investigate the effects of the symmetry energy on the neutron drip density and properties of neutron star crusts around the neutron drip point.

The nuclear symmetry energy and its density dependence play a crucial role in understanding various phenomena in nuclear physics and astrophysics [3, 13]. The symmetry energy $E_{\rm sym}$ at saturation density can be constrained by experiments to be around 30 ± 4 MeV, while the symmetry energy slope L at saturation density is still very uncertain and may vary from about 20 to 115 MeV [14]. Many properties of neutron stars, such as the crust structure, the crust-core transition, and the star radius, are sensitive to the symmetry energy and its density dependence [11, 15, 16]. In Ref. [11], the properties of nuclei in the inner crust were studied using a parametrized Thomas–Fermi approach; they were found to be sensitive to the density dependence of the symmetry energy. In Ref. [17], a self-consistent Thomas–Fermi approximation was used to calculate the properties of the inner crust including pasta phases, and it was found that L could have dramatic effects on the crust structure.

The equilibrium state of neutron star crusts can be determined by minimizing the total energy density at a given average baryon density n_b under the conditions of β equilibrium and charge neutrality. The outer crust is well described based on experimental masses of neutron-rich nuclei, but the inner crust has to be studied by using phenomenological models due to the presence of dripped neutrons. In past decades, the structure of the inner crust has

been investigated by using various methods, such as the liquid-drop model [10, 18, 19] and the Thomas–Fermi approach [11, 17, 20, 21]. Using the Wigner–Seitz approximation, the crust is divided into spherical cells, in which a nucleus is located in the center surrounded by a gas of electrons and neutrons. A simple treatment for the matter inside the Wigner–Seitz cell is referred to as the coexisting phases (CP) method [12, 20], in which the matter inside the cell separates into a dense phase and a dilute phase with a sharp interface. The two coexisting phases satisfy Gibbs conditions for phase equilibrium, which correspond to bulk equilibrium without finite-size effects. The surface and Coulomb energies are perturbatively taken into account after the coexisting phases are achieved. Another treatment of the inner crust is based on a compressible liquid-drop (CLD) model and in this treatment the equilibrium state is determined by minimization of the total energy density including the surface and Coulomb energies [18, 22, 23]. Therefore, the finite-size effects due to the surface and Coulomb energies are properly taken into account in this method. The Thomas–Fermi (TF) approximation is considered to be self-consistent in the treatment of finite-size effects and nucleon distributions and has been widely used in atomic and nuclear physics [24]. The TF approximation has been used to study neutron star crusts including pasta phases at zero temperature [17, 25] and finite temperature [21]. It is important to compare and analyze the differences between these methods and explore their validity at low density.

This paper has two aims. The first one is to analyze the differences between the methods used for the study of neutron star crusts, so as to examine the finite-size effects due to the surface and Coulomb energies in determining the equilibrium state at low density. In fact, we find that the energy density obtained in the CP method is generally larger than that of the corresponding homogeneous phase at low densities around the neutron drip point. The failure of the CP method at low densities may be due to the improper treatment of the surface and Coulomb energies. The second aim of this paper is to investigate the effects of the symmetry energy on the neutron drip density and properties of neutron star crusts. To calculate the properties of neutron star crusts, we employ the TF approximation, which is considered to be self-consistent in the treatment of finite-size effects and nucleon distributions. For the nuclear interaction, we adopt the relativistic mean-field (RMF) theory, which has been successfully used to study various phenomena in nuclear physics [26–28]. In the RMF approach, nucleons interact via the exchange of scalar and vector mesons, while the parameters are fitted to nuclear matter saturation properties or ground-state properties

of finite nuclei. We consider several different parametrizations of the RMF theory, so that we can examine the model dependence of the results obtained.

This article is arranged as follows. In Sec. II, we briefly describe the three methods used for the study of neutron star crusts, namely, the TF approximation, the CP method, and the CLD model with finite-size effects. In Sec. III, we discuss the RMF parameters to be used in this study. In Sec. IV, we show the numerical results and compare the differences between these methods, as well as discuss the effects of the symmetry energy on the neutron drip density and properties of the inner crust. Section V is devoted to the conclusions.

II. MODEL AND METHODS

We employ the RMF theory to study a system consisting of protons, neutrons, and electrons. In the RMF approach, nucleons interact via the exchange of various mesons. The mesons considered are isoscalar scalar and vector mesons (σ and ω) and the isovector vector meson (ρ). Electrons and protons interact through the electromagnetic field A^μ. The Lagrangian density reads

$$\begin{aligned}
\mathcal{L}_{\rm RMF} \;=\; & \sum_{i=p,n} \bar{\psi}_i \left\{ i\gamma_\mu \partial^\mu - (M + g_\sigma \sigma) - \gamma_\mu \left[g_\omega \omega^\mu + \frac{g_\rho}{2} \tau_a \rho^{a\mu} + \frac{e}{2} (1+\tau_3) A^\mu \right] \right\} \psi_i \\
& + \bar{\psi}_e \left[i\gamma_\mu \partial^\mu - m_e + e\gamma_\mu A^\mu \right] \psi_e \\
& + \frac{1}{2} \partial_\mu \sigma \partial^\mu \sigma - \frac{1}{2} m_\sigma^2 \sigma^2 - \frac{1}{3} g_2 \sigma^3 - \frac{1}{4} g_3 \sigma^4 \\
& - \frac{1}{4} W_{\mu\nu} W^{\mu\nu} + \frac{1}{2} m_\omega^2 \omega_\mu \omega^\mu + \frac{1}{4} c_3 \left(\omega_\mu \omega^\mu \right)^2 \\
& - \frac{1}{4} R^a_{\mu\nu} R^{a\mu\nu} + \frac{1}{2} m_\rho^2 \rho^a_\mu \rho^{a\mu} + \Lambda_{\rm v} \left(g_\omega^2 \omega_\mu \omega^\mu \right) \left(g_\rho^2 \rho^a_\mu \rho^{a\mu} \right) - \frac{1}{4} F_{\mu\nu} F^{\mu\nu},
\end{aligned} \tag{1}$$

where $W^{\mu\nu}$, $R^{a\mu\nu}$, and $F^{\mu\nu}$ are the antisymmetric field tensors for ω^μ, $\rho^{a\mu}$, and A^μ, respectively. We include the ω-ρ coupling term as described in [29], which is essential in modifying the symmetry energy slope. In the RMF approach, the meson fields are treated as classical fields and the field operators are replaced by their expectation values. For a static system, the nonvanishing expectation values are $\sigma = \langle\sigma\rangle$, $\omega = \langle\omega^0\rangle$, $\rho = \langle\rho^{30}\rangle$, and $A = \langle A^0\rangle$. From the Lagrangian density, we can derive the equations of motion for these mean fields in a uniform or nonuniform system.

We employ the Wigner–Seitz approximation to describe the nonuniform matter in neutron star crusts. In the present study, we focus on examining the symmetry energy effects on

properties of neutron star crusts around the neutron drip density, where the inhomogeneous matter is composed of spherical nuclei arranged in a body-centered-cubic (BCC) lattice. Generally, nonspherical nuclei (pasta phases) may appear only at densities higher than 0.05 fm^{-3} [11, 12]. Therefore, we consider the matter of the crust to be divided into spherical cells treated in the Wigner–Seitz approximation. The Wigner–Seitz cell has the same volume as the unit cell in the BCC lattice. The lattice constant a and the Wigner–Seitz cell radius r_{ws} are related to the cell volume by $V_{\mathrm{cell}} = a^3 = 4\pi r_{\mathrm{ws}}^3/3 = N_b/n_b$, where N_b and n_b are the baryon number per cell and the average baryon number density, respectively. We assume that each spherical nucleus is located in the center of a charge-neutral cell consisting of a gas of nucleons and electrons. It is well known that the electron screening effects are negligible at subnuclear densities [30], so we ignore the electron screening effect caused by the nonuniform charged particle distributions and assume the electron density to be uniform inside the Wigner–Seitz cell. At a given average baryon density n_b, the equilibrium state is determined by minimizing the total energy density of the system. To calculate the total energy per cell, we use the self-consistent TF approximation with the RMF model, while the CP method with Gibbs equilibrium conditions and the CLD model including finite-size effects due to the surface and Coulomb energies are adopted for comparison.

A. Thomas–Fermi approximation

In the TF approximation, the total energy per cell can be written as

$$E_{\mathrm{cell}} = \int_{\mathrm{cell}} \varepsilon_{\mathrm{rmf}}(r) d^3r + \varepsilon_e V_{\mathrm{cell}} + \Delta E_{\mathrm{bcc}}, \tag{2}$$

where ε_e denotes the electron kinetic energy density. ΔE_{bcc} is a correction term for the BCC lattice, which is negligible when the nuclear size is much smaller than the cell size [31, 32]. $\varepsilon_{\mathrm{rmf}}(r)$ is the local energy density at radial position r, which is calculated in the RMF model

as

$$
\begin{aligned}
\varepsilon_{\rm rmf} \;=\; & \sum_{i=p,n} \frac{1}{\pi^2} \int_0^{k_F^i} dk\, k^2 \sqrt{k^2 + M^{*2}} \\
& + \frac{1}{2}(\nabla\sigma)^2 + \frac{1}{2} m_\sigma^2 \sigma^2 + \frac{1}{3} g_2 \sigma^3 + \frac{1}{4} g_3 \sigma^4 \\
& - \frac{1}{2}(\nabla\omega)^2 - \frac{1}{2} m_\omega^2 \omega^2 - \frac{1}{4} c_3 \omega^4 + g_\omega \omega \left(n_p + n_n\right) \\
& - \frac{1}{2}(\nabla\rho)^2 - \frac{1}{2} m_\rho^2 \rho^2 - \Lambda_{\rm v} g_\omega^2 g_\rho^2 \omega^2 \rho^2 + \frac{g_\rho}{2} \rho \left(n_p - n_n\right) \\
& - \frac{1}{2}(\nabla A)^2 + eA \left(n_p - n_e\right), \qquad (3)
\end{aligned}
$$

where n_i is the number density of species i and $M^* = M + g_\sigma \sigma$ is the effective nucleon mass.

From the Lagrangian density (1), we obtain the equations of motion for the mean fields:

$$-\nabla^2\sigma + m_\sigma^2 \sigma + g_2 \sigma^2 + g_3 \sigma^3 = -g_\sigma \left(n_p^s + n_n^s\right), \qquad (4)$$

$$-\nabla^2\omega + m_\omega^2 \omega + c_3 \omega^3 + 2\Lambda_{\rm v} g_\omega^2 g_\rho^2 \rho^2 \omega = g_\omega \left(n_p + n_n\right), \qquad (5)$$

$$-\nabla^2\rho + m_\rho^2 \rho + 2\Lambda_{\rm v} g_\omega^2 g_\rho^2 \omega^2 \rho = \frac{g_\rho}{2} \left(n_p - n_n\right), \qquad (6)$$

$$-\nabla^2 A = e \left(n_p - n_e\right), \qquad (7)$$

where n_i^s is the scalar density of species i. The equations of motion for nucleons give the standard relations between the densities and chemical potentials,

$$\mu_p \;=\; \sqrt{\left(k_F^p\right)^2 + M^{*2}} + g_\omega \omega + \frac{g_\rho}{2} \rho + eA, \qquad (8)$$

$$\mu_n \;=\; \sqrt{\left(k_F^n\right)^2 + M^{*2}} + g_\omega \omega - \frac{g_\rho}{2} \rho. \qquad (9)$$

We note that the chemical potential is spatially constant throughout the Wigner–Seitz cell, while other quantities such as densities and mean fields depend on the position r. In the Wigner–Seitz cell of neutron star crusts, the conditions of β equilibrium and charge neutrality are imposed, which provide the constraints

$$\mu_n \;=\; \mu_p + \mu_e, \qquad (10)$$

$$N_e \;=\; N_p = \int_{\rm cell} n_p(r) d^3 r. \qquad (11)$$

At a given average baryon density n_b, we minimize the total energy density with respect to the cell radius $r_{\rm ws}$. To compute the total energy per cell at fixed $r_{\rm ws}$ and n_b, we numerically solve the coupled Eqs. (4)–(7) under the constraints (10) and (11). In practice, we start with

an initial guess for the mean fields $\sigma(r)$, $\omega(r)$, $\rho(r)$, and $A(r)$, then determine the chemical potentials μ_n, μ_p, and μ_e by the constraints (10) and (11) and the given average density $n_b = (N_p + N_n) \,/\, V_{\rm cell}$. Once the chemical potentials are obtained, we can calculate various densities and solve Eqs. (4)–(7) to get new mean fields. This procedure is iterated until convergence is achieved.

B. Coexisting phases method

In the CP method [12, 20, 25, 30], the matter inside the Wigner–Seitz cell separates into a dense phase and a dilute phase with a sharp interface. The coexisting phases satisfy Gibbs conditions for phase equilibrium, which correspond to bulk equilibrium without finite-size effects. The surface and Coulomb energies can be perturbatively taken into account after the coexisting phases are achieved. We denote the dense liquid phase and dilute gas phase by L and G, respectively. The Gibbs conditions for a nuclear liquid phase in coexistence with a neutron gas at zero temperature are written as

$$P^L = P^G, \tag{12}$$

$$\mu_n^L = \mu_n^G. \tag{13}$$

The conditions of β equilibrium and charge neutrality with a fixed average baryon density n_b provide the following constraints:

$$\mu_e \;=\; \mu_n^L - \mu_p^L, \tag{14}$$

$$n_e \;=\; n_p = u n_p^L, \tag{15}$$

$$n_b \;=\; u n_b^L + (1-u)\, n_b^G, \tag{16}$$

where u denotes the volume fraction of the liquid phase. We numerically solve Eqs. (12)–(16) within the RMF model to obtain all properties of the two coexisting phases and the volume fraction u at given density n_b.

The total energy density of the system is given by

$$\varepsilon = u\varepsilon_{\rm bulk}^L + (1-u)\,\varepsilon_{\rm bulk}^G + \varepsilon_e + \varepsilon_{\rm surf} + \varepsilon_{\rm Coul}, \tag{17}$$

where $\varepsilon_{\rm bulk}^{L(G)}$ is the bulk energy density of phase $L(G)$ obtained in the RMF model. The

surface and Coulomb energy densities for a spherical cell are given by

$$\varepsilon_{\rm surf} = \frac{3\tau u}{r_d}, \tag{18}$$

$$\varepsilon_{\rm Coul} = \frac{e^2}{5}\left(n_b^L Y_p^L\right)^2 r_d^2 u D\left(u\right), \tag{19}$$

with

$$D\left(u\right) = 1 - \frac{3}{2}u^{1/3} + \frac{1}{2}u. \tag{20}$$

Here τ is the surface tension, which can be obtained by a TF calculation for semi-infinite nuclear matter [12, 21, 33]. $e = \sqrt{4\pi/137}$ is the electromagnetic coupling constant. The radius of the droplet, r_d, is determined by minimizing $\varepsilon_{\rm surf} + \varepsilon_{\rm Coul}$, which leads to $\varepsilon_{\rm surf} = 2\varepsilon_{\rm Coul}$. The radius of the droplet and that of the Wigner–Seitz cell are, respectively, given by

$$r_d = \left[\frac{15\tau}{2e^2\left(n_b^L Y_p^L\right)^2 D(u)}\right]^{1/3}, \tag{21}$$

$$r_{\rm ws} = u^{-1/3} r_d. \tag{22}$$

We calculate the energy density of the cell by using Eq. (17) at a given average baryon density n_b and compare to that of corresponding homogeneous phase. It is believed that the nonuniform matter in the Wigner–Seitz approximation should have a smaller energy density than the homogeneous phase at low density. However, we find that the energy density obtained in the CP method is generally larger than that of the corresponding homogeneous phase around the neutron drip density. The failure of the CP method at low density may be due to the improper treatment of the surface and Coulomb energies.

C. Compressible liquid-drop model

In the CP method, the equilibrium conditions are determined by the bulk properties without finite-size effects. To incorporate the surface and Coulomb energies in determining the equilibrium conditions, we employ the CLD model to calculate the energy density of the Wigner–Seitz cell and derive the equilibrium equations by minimization of the total energy density including the surface and Coulomb contributions [18, 22, 23]. The energy density of the cell is generally expressed as a function of the following six variables: the volume

fraction and radius of the droplet (u and r_d), the baryon density and proton fraction inside the droplet (n_b^L and Y_p^L), and the number densities of the neutron and electron gases (n_b^G and n_e). The total energy density of the cell is given by

$$\varepsilon = u\varepsilon_{\rm bulk}(n_b^L, Y_p^L) + (1-u)\,\varepsilon_{\rm bulk}(n_b^G, 0) + \varepsilon_e(n_e) + \varepsilon_{\rm surf}(u, r_d, \tau) + \varepsilon_{\rm Coul}(u, r_d, n_b^L, Y_p^L), \quad (23)$$

where $\varepsilon_{\rm bulk}(n_b^i, Y_p^i)$ is the energy density of homogeneous nuclear matter in phase i ($i = L, G$), which can be calculated in the RMF model. The surface and Coulomb terms are given by Eqs. (18) and (19), respectively. Under the constraints of charge neutrality and fixed average baryon density given by Eqs. (15) and (16), there are only four independent variables and we may choose u, r_d, n_b^L, and Y_p^L. Therefore, n_e and n_b^G are related to the independent variables by

$$n_e = u n_b^L Y_b^L, \quad (24)$$

$$n_b^G = \frac{n_b - u n_b^L}{1-u}. \quad (25)$$

By minimizing the total energy density with respect to the independent variables [23], we obtain the following equilibrium equations:

$$0 = \frac{\partial \varepsilon}{\partial r_d} \;:\quad r_d = \left[\frac{15\tau}{2e^2\left(n_b^L Y_p^L\right)^2 D(u)}\right]^{1/3}, \quad (26)$$

$$0 = \frac{1}{u n_b^L}\frac{\partial \varepsilon}{\partial Y_p^L} \;:\quad \mu_e = \mu_n^L - \mu_p^L - \frac{2e^2}{5} n_b^L Y_p^L r_d^2 D(u), \quad (27)$$

$$0 = \frac{\partial \varepsilon}{\partial n_b^L} - \frac{Y_p^L}{n_b^L}\frac{\partial \varepsilon}{\partial Y_p^L} \;:\quad \mu_n^L = \mu_n^G, \quad (28)$$

$$0 = \frac{n_b^L}{u}\frac{\partial \varepsilon}{\partial n_b^L} - \frac{\partial \varepsilon}{\partial u} \;:\quad P^L - P^G = \frac{e^2}{5}\left(n_b^L Y_p^L\right)^2 r_d^2\left(1 - 2u^{1/3} + u\right). \quad (29)$$

We note that the terms involving derivatives of the surface tension are ignored in deriving these equilibrium equations. As discussed by Iida and Oyamatsu [34], the surface tension τ may depend on the inner density and proton fraction (n_b^L and Y_p^L). Furthermore, τ could be affected by the size of the droplet (r_d), which is known as a curvature correction to the surface tension [5]. However, the dependence of τ on these variables is poorly known, especially in a neutron-rich system. This is because the surface tension is generally obtained by a TF calculation for semi-infinite nuclear matter. Due to the equilibrium conditions between the nuclear liquid and gas phases, the surface tension would be a function of only

one of the four variables n_b^L, Y_p^L, n_b^G, and Y_p^G. Therefore, it is not possible to obtain the partial derivatives of τ with respect to each independent variable from this calculation. For simplicity, we neglect contributions from the derivatives of the surface tension in deriving the above equilibrium equations. One can see that equilibrium equations (26)–(29) of the present paper are equivalent to Eqs. (43)–(47) of Ref. [1].

By comparing Eq. (27) with Eq. (14), we can see that the β equilibrium condition is altered due to the inclusion of finite-size effects in the minimization procedure. The last term of Eq. (27) comes from the Coulomb energy, which favors a smaller electron chemical potential. This leads to the conclusion that the electron fraction (equal to the average proton fraction) is overestimated in the CP method with bulk equilibrium. Also, the inclusion of finite-size effects affects the mechanical equilibrium as can be seen by comparing Eq. (29) with Eq. (12). The last term of Eq. (29) comes from the sum of the surface and Coulomb energies. Generally, the bulk pressure inside the droplet is larger than that outside due to the surface and Coulomb contributions, which leads to a higher density at the center of the droplet.

III. PARAMETERS

In this section, we discuss the choice of the RMF parameters to be used in this study. The parameters of the RMF models are generally fitted to nuclear matter saturation properties or ground-state properties of finite nuclei. To study the properties of neutron star crusts and compare the differences among various methods, we consider four different RMF parametrizations, NL3 [35], TM1 [36], FSU [29], and IUFSU [37], so that we can examine the model dependence of the results obtained. These RMF models are known to be successful in reproducing the ground state properties of finite nuclei including unstable ones. The NL3 parametrization includes nonlinear terms of the σ meson only, while the TM1 parametrization includes nonlinear terms for both σ and ω mesons. An additional ω-ρ coupling term is added in the FSU and IUFSU parametrizations, and it plays an important role in modifying the density dependence of the symmetry energy and affecting the neutron star properties [16, 29, 37–40]. The IUFSU parametrization was developed from FSU by reducing the neutron skin thickness of ^{208}Pb and increasing the maximum neutron star mass in the parameter fitting [37]. The TM1 model was successfully used to construct the equation of

state for supernova simulations and neutron star calculations [32, 41]. For completeness, we present the parameters and saturation properties of these RMF models in Table I.

In order to examine the influence of the symmetry energy slope L, we generate two sets of models based on the TM1 and IUFSU parametrizations. We determine the model parameters by simultaneously adjusting g_ρ and $\Lambda_{\rm v}$ so as to achieve a given L at saturation density and keep $E_{\rm sym}$ fixed at a density of 0.11 fm^{-3}. The choice of the fixed density $n_{\rm fix} = 0.11\,{\rm fm}^{-3}$ is based on the following consideration. In one set of generated models, the variation of L at saturation density would not affect the reproduction of well-known properties of finite nuclei. It has been pointed out that the binding energy of finite nuclei is essentially determined by the symmetry energy at a density of $\sim 0.11\,{\rm fm}^{-3}$, not by the symmetry energy at saturation density [14, 38]. To examine the sensitivity of the binding energy to the fixed density $n_{\rm fix}$ of the symmetry energy, we perform a standard RMF calculation as described in Refs. [27, 36] for ^{208}Pb using the two sets of generated models with different choices of $n_{\rm fix}$. One can see in Fig. 1 that the binding energy per nucleon of ^{208}Pb remains almost unchanged with varying L using $n_{\rm fix} = 0.11\,{\rm fm}^{-3}$, whereas it deviates from the experimental value (7.87 MeV) using $n_{\rm fix} = 0.10\,{\rm fm}^{-3}$ or $n_{\rm fix} = n_0$ (where n_0 is the saturation density). In Tables II and III, we present the parameters g_ρ and $\Lambda_{\rm v}$ generated based on TM1 and IUFSU by producing a given L at saturation density and fixed symmetry energy at $n_{\rm fix} = 0.11\,{\rm fm}^{-3}$. We also show in these tables the symmetry energy at saturation density, $E_{\rm sym}(n_0)$, and the neutron-skin thickness $\Delta r_{np} = \langle r_n^2\rangle^{1/2} - \langle r_p^2\rangle^{1/2}$ of ^{208}Pb, both of which generally increase with increasing L. We stress that all models in each set have the same isoscalar saturation properties and fixed symmetry energy at $n_{\rm fix} = 0.11\,{\rm fm}^{-3}$, but they have different symmetry energy slope L. By using the set of models with different L, it is possible to study the impact of L on the neutron drip density and properties of neutron star crusts.

IV. RESULTS AND DISCUSSION

In this section, we investigate the effects of the symmetry energy on the neutron drip density and properties of neutron star crusts. We first make a detailed comparison among the three methods used for the study of neutron star crusts, namely, the TF approximation, the CP method, and the CLD model with finite-size effects. We analyze the differences among these methods and explore their validity at low densities near the neutron drip point.

To study the influence of the symmetry energy slope L, we employ the TF approximation, which is considered to be self-consistent in the treatment of finite-size effects and nucleon distributions.

A. Comparison between different methods

To describe nonuniform matter in the Wigner–Seitz cell, we consider three different methods: (1) the simple CP method with bulk Gibbs equilibrium conditions; (2) the CLD model with equilibrium conditions determined by including the surface and Coulomb energies; and (3) the self-consistent TF approximation. We note that treatments of surface and Coulomb energies are obviously different among these methods. In the CP method, Gibbs equilibrium conditions are used which correspond to bulk equilibrium without finite-size effects, while the surface and Coulomb energies are perturbatively incorporated after the two coexisting phases are achieved. In the CLD model, equilibrium conditions are determined by minimization of the total energy density including the surface and Coulomb energies; therefore they are incorporated in a consistent manner. In the TF approximation, the surface effect and nucleon distributions are treated self-consistently, rather than a sharp surface being assumed in the CP and CLD methods. In addition, a neutron skin can be well described within the TF approximation, but it is not explicitly included in the CP and CLD methods.

In Fig. 2, we show the total energy per nucleon, $E = \varepsilon/n_b - M$, as a function of the average baryon density n_b obtained using the TF, CLD, and CP methods, while that of homogeneous matter is also displayed. It is interesting to see that the three methods yield very similar E at higher densities, but there are significant differences at lower densities. Moreover, one can see that the simple CP method fails to describe the nonuniform matter near the neutron drip density, since E of CP is larger than that of homogeneous matter. We note that the kinks of CP at $n_b < 10^{-3}$ fm^{-3} correspond to the neutron drip point. The failure of the CP method may be due to its improper treatment of the surface and Coulomb energies. It implies that the finite-size effect due to the surface and Coulomb energies is too large to be treated perturbatively at low densities, so that we have to include contributions from surface and Coulomb energies in determining the equilibrium state as done in the CLD and TF methods. By comparing the results between CLD and CP, one can see an obvious improvement due to the inclusion of finite-size effects in the CLD method.

Furthermore, the results of CLD are very close to those obtained in the self-consistent TF calculation. In order to analyze the results of Fig. 2, we plot various contributions to E in Fig. 3. The Coulomb energy per nucleon, $E_{\rm Coul} = \varepsilon_{\rm Coul}/n_b$, is calculated by using Eq. (19) in the CP and CLD methods, while it can be easily computed in the TF approximation by using $E_{\rm Coul} = \frac{1}{2N_b}\int_{\rm cell} eA(r)\left[n_p(r) - n_e\right] d^3r$. However, it is difficult to separate the surface energy from the bulk energy in the TF approximation, because both are involved in Eq. (3). To estimate the surface energy in the TF approximation, we use the equilibrium condition $\varepsilon_{\rm surf} = 2\,\varepsilon_{\rm Coul}$ obtained in the liquid-drop model, which yields the sum $\varepsilon_{\rm surf} + \varepsilon_{\rm Coul} = 3\,\varepsilon_{\rm Coul}$. Therefore, we can define the bulk energy density in the TF approximation by $\varepsilon_{\rm bulk} = \left(E_{\rm cell} - \Delta E_{\rm bcc}\right)/V_{\rm cell} - 3\varepsilon_{\rm Coul} - \varepsilon_e$ according to Eq. (2), while it is given by $\varepsilon_{\rm bulk} = u\varepsilon^L_{\rm bulk} + (1-u)\,\varepsilon^G_{\rm bulk}$ in the CP and CLD methods. In Fig. 3, from top to bottom, we show, respectively, the bulk energy per nucleon, $E_{\rm bulk} = \varepsilon_{\rm bulk}/n_b - M$, the electron kinetic energy per nucleon, $E_e = \varepsilon_e/n_b$, and the Coulomb energy per nucleon, $E_{\rm Coul}$, obtained in the CP, CLD, and TF methods using the TM1 parametrization. One can see that E_e and $E_{\rm Coul}$ increase with decreasing n_b, and the differences between CP and CLD methods become very large at low density. Due to the increasing contributions of E_e and $3E_{\rm Coul}$ (the sum of surface and Coulomb energies per nucleon), the total energy per nucleon, E, obtained in the CP method is even larger than that of homogeneous matter near the neutron drip density (see Fig. 2), which implies that the simple CP method is not applicable to describing nonuniform matter at low density. In order to understand the differences in E_e and $E_{\rm Coul}$ between the CP and CLD methods, we display the electron fraction $Y_e = n_e/n_b$ as a function of n_b in Fig. 4. At a given n_b, a large Y_e corresponds to large n_e and μ_e, which results in more contributions from E_e and $E_{\rm Coul}$. One can see that Y_e of the CP method is significantly larger than that of the CLD and TF methods in all cases of Fig. 4. This can be understood by comparing Eqs. (14) and (27). In the CP method, μ_e is determined by using Eq. (14), while an additional term (the last term) appears in Eq. (27) caused by the Coulomb energy in the CLD method. This term leads to a smaller μ_e in the CLD method compared to the CP case. Therefore, we conclude that the inclusion of surface and Coulomb energies in determining the equilibrium state plays a crucial role in the description of nonuniform matter at low density.

In Fig. 5, we plot the radius of the droplet, r_d, and that of the Wigner–Seitz cell, $r_{\rm ws}$, as a function of n_b obtained by using the TF, CLD, and CP methods. In the CP and

CLD methods, r_d is given by Eq. (21), while it is defined by $r_d = \sqrt{\frac{5}{3}}\langle r_p^2\rangle^{1/2}$ in the TF approximation. One can see that r_d does not explicitly depend on n_b and there is no significant difference among the three methods. This is because the equilibrium nuclear size r_d is mainly determined by a competition between the surface and Coulomb energies, which is a common feature in these methods. On the other hand, $r_{\rm ws}$ obviously decreases with increasing n_b. Moreover, $r_{\rm ws}$ in the CP method is generally smaller than that of the CLD and TF methods. This tendency is related to the behavior of Y_e shown in Fig. 4. As discussed above, a large Y_e corresponds to large n_e and μ_e, which results in a large volume fraction u and a small $r_{\rm ws}$ according to the relations given in Eqs. (15) and (22). In Fig. 6, we present the proton number Z of the droplet as a function of n_b obtained by using the TF, CLD, and CP methods. It is well known that Z is sensitive to the surface energy [11]. We can see that the density dependence of Z is relatively weak at low density for all cases, while it shows a strong density dependence with increasing n_b. The behavior of IUFSU is different from others due to its relatively low value of L. It has been shown in Refs. [11, 12] that a small L favors a large surface tension τ, which leads to a large Z since Z increases monotonically with τ. Comparing results among the three methods, we find that Z of the TF method is generally larger than that of the CP and CLD methods. This may be due to the different treatment of nucleon distributions. In the TF approximation, the surface effect and nucleon distributions are calculated self-consistently and the neutron skin is well described.

B. Neutron drip density

We perform the self-consistent TF calculation to study the effects of the symmetry energy on the neutron drip density. To examine the influence of the symmetry energy slope L, we use two sets of models generated from the TM1 and IUFSU parametrizations. We note that all models in each set have the same isoscalar saturation properties and fixed symmetry energy at $n_{\rm fix} = 0.11\,{\rm fm}^{-3}$, but they have different symmetry energy slope L. The neutron drip point is determined by the condition $\mu_n = Mc^2$. Beyond this point, neutrons begin to drip out of the nuclei and form a free neutron gas. In Fig. 7, we show the neutron drip density $n_{\rm drip}$ as a function of L using the two sets of models generated from TM1 and IUFSU, while the results of NL3 and FSU are also displayed. It is found that $n_{\rm drip}$ increases with L in

both TM1 and IUFSU cases. This tendency can be understood from the following analysis. The neutron drip density is related to the nucleon number and radius of the Wigner–Seitz cell as $n_{\rm drip} = A/\frac{4}{3}\pi r_{\rm ws}^3$. The nucleon number A at $n_{\rm drip}$ is not obviously affected by L [see Fig. 9(a)]. However, the cell radius $r_{\rm ws}$ at $n_{\rm drip}$ decreases significantly with increasing L, as shown in Fig. 8. One reason for the decrease of $r_{\rm ws}$ is because the generated models in each set have fixed symmetry energy at $n_{\rm fix} = 0.11\,{\rm fm}^{-3}$ with different L, and, therefore, a larger L corresponds to a larger symmetry energy $E_{\rm sym}$ near the saturation density (see Tables II and III). Based on the relation derived from the liquid-drop model, $\mu_e = \mu_n^L - \mu_p^L \simeq 4\delta E_{\rm sym}$ with $\delta = 1 - 2Y_p^L$ being the neutron excess, a large $E_{\rm sym}$ at the center of the nucleus (corresponding to a large value of L) favors a high μ_e, although it corresponds to a small δ and a low nucleon density in the center region (see Fig. 10). As mentioned above, a high value of μ_e results in a large volume fraction u and a small $r_{\rm ws}$ according to the relations given in Eqs. (15) and (22). Therefore, a larger L in one set of generated models leads to a smaller $r_{\rm ws}$ and a larger $n_{\rm drip}$, as shown in Figs. 7 and 8. The L dependence of $n_{\rm drip}$ can also be explained by the behavior of the neutron chemical potential μ_n. At the average baryon density n_b, a small L generally corresponds to a high μ_n due to the large contribution from the ρ meson [see Fig. 13(b)]. Therefore, the model with a smaller L can reach the threshold condition for the neutron drip $\mu_n = Mc^2$ at a lower density, which implies an increasing $n_{\rm drip}$ with L, as shown in Fig. 7.

We display in Fig. 9 some properties of the nucleus at the neutron drip density as a function of L obtained in the TF calculation. As one can see from Fig. 9(a), the nucleon number A of the equilibrium nucleus is almost independent of L. This is because the generated models with different L have fixed symmetry energy at $n_{\rm fix} = 0.11\,{\rm fm}^{-3}$, which can produce very similar binding energies for finite nuclei within one set of generated models (see Fig. 1). The proton number Z slightly decreases with increasing L, which can be understood from the L dependence of the surface tension. As discussed in Refs. [11, 12, 17], a small L favors a large surface tension τ, which leads to a large Z since Z increases monotonically with τ. The average proton fraction Z/A of the nucleus is found to decrease with increasing L [see Fig. 9(b)], which is caused by the decrease of Z with L. The root-mean-square (rms) radius of the neutron (R_n) increases with L, whereas that of the proton (R_p) decreases [see Fig. 9(c)]. The difference between R_n and R_p, known as the neutron skin thickness (Δr_{np}), is displayed in Fig. 9(d). It is well known that a larger L results in a thicker neutron

skin [17, 37–39, 42], which is also observed in Fig. 9(d).

We plot in Fig. 10 the nucleon density distributions in the Wigner–Seitz cell at the neutron drip density obtained with two extreme values of L in the set of TM1. It is shown that the nucleon distributions, especially the neutron distributions, can be significantly affected by the value of L. One can see that a large L results in a small nucleon density at the center of the cell. This may be understood from the analysis based on a liquid-drop model. As discussed by Iida and Oyamatsu [34], the equilibrium density of the nucleon liquid can be estimated by the condition of zero pressure when there is no neutron gas outside. The bulk pressure vanishes at $n_b^L = n_0 - \frac{3Ln_0}{K}\delta^2$ derived from the liquid-drop model [34]. This implies that the equilibrium density n_b^L decreases with increasing L for a fixed neutron excess δ. On the other hand, a larger L in one set of generated models corresponds to a larger symmetry energy $E_{\rm sym}$ near the saturation density, as mentioned above. As a result, a larger L favors fewer neutrons (equivalent to a smaller δ) in the central region of the nucleus due to its larger $E_{\rm sym}$. Meanwhile, more neutrons are distributed in the surface region due to its smaller $E_{\rm sym}$ for a larger L at very low density. Therefore, a large value of L results in relatively large neutron rms radius and neutron skin thickness [see Figs. 9(c) and 9(d)].

C. Properties of nuclei in neutron star crusts

We employ the TF approximation to study the effects of the symmetry energy on properties of nuclei in the inner crust. Above the neutron drip density $n_{\rm drip}$, a gas of free neutrons coexists with a lattice of spherical nuclei, and the equilibrium nuclei become more and more neutron rich as the density increases. In Fig. 11, we display the droplet proton number Z, nucleon number A_d, and proton fraction Z/A_d as a function of the average baryon density n_b using the two sets of generated models. The droplet nucleon number A_d is defined by subtracting the background neutrons in order to isolate the nucleus from a surrounding neutron gas [17, 43]. It is shown that Z and A_d weakly depend on n_b at lower densities, while they rapidly change at relatively high densities. For the L dependence of Z and A_d, it is found that Z decreases monotonically with increasing L, while A_d is almost independent of L at low densities. These behaviors are consistent with those shown in Fig. 9(a). Our results are very similar to those reported in Ref. [17]. The L dependence of Z may be understood from the behavior of the surface tension τ. Based on the size equilibrium condition of the

liquid-drop model, $\varepsilon_{\rm surf} = 2\,\varepsilon_{\rm Coul}$, a large value of τ leads to large nuclear size r_d and proton number Z. It has been shown in Refs. [11, 12, 17] that a large L corresponds to a small τ. Therefore, a small Z is achieved for a large L due to its small τ. The L dependence of A_d at high densities is mainly because the nuclear size increases with decreasing L (equivalent to increasing τ). The proton fraction Z/A_d at low densities is found to decrease with increasing L, which is related to the behaviors of Z and A_d, but the opposite tendency is observed at high densities. A similar behavior of Z/A_d was also observed in Fig. 4(f) of Ref. [17]. The strong L dependence at high densities obtained in the present TF calculation is consistent with that shown in our previous study using the CP method [12], where a large value of L leads to small τ, Z, A_d, and r_d values (see Figs. 4–7 of Ref. [12]). It has been shown in Sec. IV A that the difference between the TF and CP methods is relatively small in the high-density region.

In Figs. 12 and 13, we present equilibrium properties of the Wigner–Seitz cell as a function of n_b obtained in the TF approximation using the two sets of generated models. For clarity of presentation, we show chemical potentials μ_e, μ_n, and μ_p in Fig. 13 with only the smallest and largest values of L in each set of generated models. One can see from Fig. 12(a) that the radius of the Wigner–Seitz cell, $r_{\rm ws}$, significantly decreases with increasing n_b, while the proton rms radius R_p weakly depends on n_b only at high densities. These behaviors are consistent with those shown in Fig. 5, where the droplet radius r_d in the TF approximation is calculated from the proton rms radius R_p as $r_d = \sqrt{\frac{5}{3}} R_p$. The decrease of $r_{\rm ws}$ is caused by the increase of nuclear volume fraction u with increasing n_b. On the other hand, the proton density at the center of the cell, $n_p(0)$, obviously decreases with increasing n_b [see Fig. 12(c)]. This is because the matter gets more neutron rich and the difference between the neutron and proton chemical potentials, which is equivalent to the electron chemical potential as $\mu_e = \mu_n - \mu_p$, becomes larger as the density increases [see Fig. 13(a)]. Moreover, the decrease of $n_p(0)$ at high densities shows a strong L dependence; namely, a small L leads to a rapid decrease of $n_p(0)$. This may be understood from the influence of the ω-ρ coupling term, which plays an important role in neutron-rich matter. At the center of the cell, we have the following relation between densities and chemical potentials according to

Eqs. (6)–(10):

$$\mu_e = \mu_n - \mu_p = \sqrt{\left(k_F^n\right)^2 + M^{*2}} - \sqrt{\left(k_F^p\right)^2 + M^{*2}} - eA - g_\rho \rho$$
$$\simeq \frac{(3\pi^2)^{2/3}}{2M^*}\left(n_n^{2/3} - n_p^{2/3}\right) - eA + \frac{g_\rho^2}{2\left(m_\rho^2 + 2\Lambda_{\rm v} g_\omega^2 g_\rho^2 \omega^2\right)}\left(n_n - n_p\right). \quad (30)$$

As n_b increases, $\mu_e = \mu_n - \mu_p$ increases monotonically, as shown in Fig. 13(a), which yields increasing $n_n(0) - n_p(0)$ and decreasing $n_p(0)$ [see Figs. 12(b) and 12(c)]. One can see from Tables II and III that the model with a small L has relatively large $\Lambda_{\rm v}$ and g_ρ. Hence, the last term of Eq. (30) can make a more significant contribution in the case of small L, which may be the main reason for the high μ_e and the rapid decrease of $n_p(0)$, corresponding to small L at high densities [see Figs. 13(a) and 12(c)]. Furthermore, large $\Lambda_{\rm v}$ and g_ρ, corresponding to small L, results in high μ_n and low μ_p, as shown in Figs. 13(b) and 13(c). For the neutron density at the center, $n_n(0)$, and that at the boundary, $n_n(r_{\rm ws})$, plotted in Fig. 12(b), it is seen that the model with a larger L predicts smaller $n_n(0)$ and larger $n_n(r_{\rm ws})$, which are more pronounced at high densities. The behaviors of $n_n(0)$ and $n_n(r_{\rm ws})$ obtained in the present study are consistent with those reported in Refs. [11, 17]. The L dependence of $n_n(0)$ and $n_n(r_{\rm ws})$ can be understood from the density dependence of the symmetry energy $E_{\rm sym}$. In one set of generated models, $E_{\rm sym}$ has the same value at $n_{\rm fix} = 0.11\,{\rm fm}^{-3}$ for different L. However, a larger L in one set of generated models corresponds to a larger $E_{\rm sym}$ at higher density in the center region and to a smaller $E_{\rm sym}$ at lower density in the neutron gas outside. Therefore, a larger L favors a more diffuse neutron distribution, which results in smaller $n_n(0)$ and larger $n_n(r_{\rm ws})$, as shown in Fig. 12(b). This tendency can be seen more clearly in Fig. 14, in which the density profiles are plotted with two extreme values of L in the set of TM1 at several average baryon densities. We conclude that a larger L in one set of generated models predicts a higher neutron drip density $n_{\rm drip}$ due to its lower neutron chemical potential μ_n. Moreover, with increasing density, neutrons drip out more easily for the model with a larger L due to its lower $E_{\rm sym}$ in the dilute neutron gas. As a result, a larger value of L predicts a higher neutron gas density $n_n(r_{\rm ws})$ in the high-density region.

We show in Fig. 14 the density distributions of neutrons and protons in the Wigner–Seitz cell at different average baryon density n_b with two extreme values of L in the set of TM1. As n_b increases, $r_{\rm ws}$ clearly decreases and the neutron density outside becomes much larger. On the other hand, the proton density at the center decreases significantly with increasing n_b, while the neutron density at the center does not change very much for different n_b. However,

the distributions of protons and neutrons become more diffuse at higher density. One can see that the differences between $L = 40$ MeV and $L = 110.8$ MeV significantly increase with increasing n_b. The nuclear size obtained with $L = 40$ MeV is larger than that with $L = 110.8$ MeV, especially for the case of $n_b = 0.05\,\mathrm{fm}^{-3}$, which leads to larger Z and A_d, as shown in Fig. 11. Furthermore, the neutron distributions with $L = 110.8$ MeV are more diffuse than those with $L = 40$ MeV, which can be explained by the density dependence of the symmetry energy E_{sym}, as discussed above. It is clearly seen that the neutron gas density with $L = 110.8$ MeV increases more rapidly than that with $L = 40$ MeV, which is also observed in Fig. 12(b). Since the Coulomb interaction is self-consistently taken into account in the TF approximation, it is seen that the proton distributions are influenced by the Coulomb potential; namely, the proton densities at the center of the cell are slightly lower than those at the surface region due to the repulsive Coulomb potential.

V. CONCLUSIONS

We have investigated the effects of the symmetry energy on the neutron drip density and properties of nuclei in neutron star crusts. The Wigner–Seitz approximation has been employed to describe the nonuniform matter around the neutron drip density. For the nuclear interaction, we have adopted the RMF theory with several successful parametrizations. We have considered and compared three different methods for calculating properties of neutron star crusts, namely, the self-consistent TF approximation, the simple CP method with bulk Gibbs equilibrium conditions, and the CLD model with equilibrium conditions determined by including the surface and Coulomb energies. It has been found that the simple CP method fails to describe the nonuniform matter around the neutron drip density due to its higher energies than that of homogeneous matter. The failure of the CP method is mainly because the finite-size effects due to the surface and Coulomb energies are too large to be treated perturbatively at low densities, so that they should be included self-consistently in determining the equilibrium state, as done in the CLD and TF methods. The results of the CLD method have been greatly improved by the inclusion of finite-size effects compared to those of the CP method. We have made a detailed comparison of the three methods and concluded that the inclusion of surface and Coulomb energies in determining the equilibrium state plays a crucial role in the description of nonuniform matter at low density.

We have examined the influence of the symmetry energy slope L using two sets of models generated from the TM1 and IUFSU parametrizations. All models in each set have the same isoscalar saturation properties and fixed symmetry energy at $n_{\rm fix} = 0.11\,{\rm fm}^{-3}$, but they have different symmetry energy slope L. The choice of $n_{\rm fix} = 0.11\,{\rm fm}^{-3}$ can produce very similar binding energies for finite nuclei within one set of generated models. We have performed the self-consistent TF calculation to study the influence of the symmetry energy slope L on the neutron drip density $n_{\rm drip}$. It has been found that $n_{\rm drip}$ increases with increasing L, which is related to the decrease of the Wigner–Seitz cell radius. At the neutron drip point, the proton fraction of the equilibrium nucleus is found to decrease with increasing L, while the neutron skin thickness shows an obvious increase with increasing L. The L dependence of the equilibrium nucleus at the neutron drip density is qualitatively consistent with that obtained in finite-nuclei calculations.

We have studied the effects of the symmetry energy on properties of nuclei in the inner crust within the TF approximation. It has been found that the proton number Z and the nucleon number A_d of the droplet weakly depend on the average baryon density n_b in the low-density region, while they rapidly change at relatively high densities. For the L dependence of Z and A_d, it has been shown that Z decreases monotonically with increasing L, while A_d is almost independent of L at low densities. On the other hand, a strong L dependence has been observed for properties of the equilibrium nucleus at high densities. The results obtained in the present self-consistent TF calculation are qualitatively consistent with those found in the literature [11, 12, 17]. We note that nuclear shell and paring effects have been neglected in the present work. It would be interesting to consider these effects in future studies.

Acknowledgment

This work was supported in part by the National Natural Science Foundation of China (Grant No. 11375089).

[1] N. Chamel and P. Haensel, Living Rev. Relativity **11**, 10 (2008).

[2] H. Heiselberg and M. Hjorth-Jensen, Phys. Rep. **328**, 237 (2000).

[3] J. M. Lattimer and M. Prakash, Phys. Rep. **442**, 109 (2007).

[4] A. W. Steiner, Phys. Rev. C **77**, 035805 (2008).

[5] F. Douchin, P. Haensel, and J. Meyer, Nucl. Phys. A **665**, 419 (2000).

[6] F. Douchin and P. Haensel, Astron. Astrophys. **380**, 151 (2001).

[7] A. Y. Potekhin, A. F. Fantina, N. Chamel, J. M. Pearson, and S. Goriely, Astron. Astrophys. **560**, A48 (2013).

[8] M. Okamoto, T. Maruyama, K. Yabana, and T. Tatsumi, Phys. Rev. C **88**, 025801 (2013).

[9] D. G. Ravenhall, C. J. Pethick, and J. R. Wilson, Phys. Rev. Lett. **50**, 2066 (1983).

[10] G. Watanabe, K. Iida, and K. Sato, Nucl. Phys. A **676**, 455 (2000).

[11] K. Oyamatsu and K. Iida, Phys. Rev. C **75**, 015801 (2007).

[12] S. S. Bao and H. Shen, Phys. Rev. C **89**, 045807 (2014).

[13] B. A. Li, L. W. Chen, and C. M. Ko, Phys. Rep. **464**, 113 (2008).

[14] Z. Zhang and L. W. Chen, Phys. Lett. B **726**, 234 (2013).

[15] C. Ducoin, J. Margueron, C. Providência, and I. Vidana, Phys. Rev. C **83**, 045810 (2011).

[16] R. Cavagnoli, D. P. Menezes, and C. Providência, Phys. Rev. C **84**, 065810 (2011).

[17] F. Grill, C. Providência, and S. S. Avancini, Phys. Rev. C **85**, 055808 (2012).

[18] G. Baym, H. A. Bethe, and C. J. Pethick, Nucl. Phys. A **175**, 225 (1971).

[19] D. G. Ravenhall, C. D. Bennett, and C. J. Pethick, Phys. Rev. Lett. **28**, 978 (1972).

[20] S. S. Avancini, D. P. Menezes, M. D. Alloy, J. R. Marinelli, M. M. W. Moraes, and C. Providência, Phys. Rev. C **78**, 015802 (2008).

[21] S. S. Avancini, S. Chiacchiera, D. P. Menezes, and C. Providência, Phys. Rev. C **82**, 055807 (2010); **85**, 059904(E) (2012).

[22] J. M. Lattimer, C. J. Pethick, D. G. Ravenhall, and D. Q. Lamb, Nucl. Phys. A **432**, 646 (1985).

[23] J. M. Lattimer and F. D. Swesty, Nucl. Phys. A **535**, 331 (1991).

[24] M. Centelles, P. Schuck, and X. Viñas, Ann. Phys. (NY) **322**, 363 (2007).

[25] S. S. Avancini, L. Brito, J. R. Marinelli, D. P. Menezes, M. M. W. deMoraes, C. Providência,

and A. M. Santos, Phys. Rev. C **79**, 035804 (2009).

[26] B. D. Serot and J. D. Walecka, Adv. Nucl. Phys. **16**, 1 (1986).

[27] Y. K. Gambhir, P. Ring, and A. Thimet, Ann. Phys. (N.Y.) **198**, 132 (1990).

[28] J. Meng, H. Toki, S. G. Zhou, S. Q. Zhang, W. H. Long, and L. S. Geng, Prog. Part. Nucl. Phys. **57**, 470 (2006).

[29] B. G. Todd-Rutel and J. Piekarewicz, Phys. Rev. Lett. **95**, 122501 (2005).

[30] T. Maruyama, T. Tatsumi, D. N. Voskresensky, T. Tanigawa, and S. Chiba, Phys. Rev. C **72**, 015802 (2005).

[31] K. Oyamatsu, Nucl. Phys. A **561**, 431 (1993).

[32] H. Shen, H. Toki, K. Oyamatsu, and K. Sumiyoshi, Astrophys. J. Suppl. **197**, 20 (2011).

[33] M. Centelles, M. Del Estal, and X. Viñas, Nucl. Phys. A **635**, 193 (1998).

[34] K. Iida and K. Oyamatsu, Phys. Rev. C **69**, 037301 (2004).

[35] G. A. Lalazissis, J. König, and P. Ring, Phys. Rev. C **55**, 540 (1997).

[36] Y. Sugahara and H. Toki, Nucl. Phys. A **579**, 557 (1994).

[37] F. J. Fattoyev, C. J. Horowitz, J. Piekarewicz, and G. Shen, Phys. Rev. C **82**, 055803 (2010).

[38] C. J. Horowitz and J. Piekarewicz, Phys. Rev. Lett. **86**, 5647 (2001).

[39] J. Carriere, C. J. Horowitz, and J. Piekarewicz, Astrophys. J. **593**, 463 (2003).

[40] C. Providência and A. Rabhi, Phys. Rev. C **87**, 055801 (2013).

[41] H. Shen, Phys. Rev. C **65**, 035802 (2002).

[42] M. Centelles, X. Roca-Maza, X. Viñas, and M. Warda, Phys. Rev. C **82**, 054314 (2010).

[43] T. Sil, J. N. De, S. K. Samaddar, X. Viñas, M. Centelles, B. K. Agrawal, and S. K. Patra, Phys. Rev. C **66**, 045803 (2002).

TABLE I: Parameter sets used in this work and corresponding nuclear matter properties at saturation density. The masses are given in MeV.

Model	NL3	TM1	FSU	IUFSU
M	939.0	938.0	939.0	939.0
m_σ	508.194	511.198	491.500	491.500
m_ω	782.5	783.0	782.5	782.5
m_ρ	763.0	770.0	763.0	763.0
g_σ	10.2170	10.0289	10.5924	9.9713
g_ω	12.8680	12.6139	14.3020	13.0321
g_ρ	8.9480	9.2644	11.7673	13.5900
g_2 (fm^{-1})	-10.4310	-7.2325	-4.2771	-8.4929
g_3	-28.885	0.6183	49.8556	0.4877
c_3	0.0000	71.3075	418.3943	144.2195
Λ_v	0.000	0.000	0.030	0.046
n_0 (fm^{-3})	0.148	0.145	0.148	0.155
E_0 (MeV)	-16.3	-16.3	-16.3	-16.4
K (MeV)	272	281	230	231
E_sym (MeV)	37.4	36.9	32.6	31.3
L (MeV)	118.2	110.8	60.5	47.2

TABLE II: Parameters g_ρ and $\Lambda_{\rm v}$ generated from the TM1 model for different slope L at saturation density n_0 with fixed symmetry energy $E_{\rm sym} = 28.05$ MeV at $n_{\rm fix} = 0.11\,{\rm fm}^{-3}$. The last two lines show the symmetry energy at saturation density, $E_{\rm sym}(n_0)$, and the neutron-skin thickness of ^{208}Pb, Δr_{np}. The original TM1 model has $L = 110.8$ MeV.

L (MeV)	40.0	50.0	60.0	70.0	80.0	90.0	100.0	110.8
g_ρ	13.9714	12.2413	11.2610	10.6142	10.1484	9.7933	9.5114	9.2644
$\Lambda_{\rm v}$	0.0429	0.0327	0.0248	0.0182	0.0128	0.0080	0.0039	0.0000
$E_{\rm sym}(n_0)$ (MeV)	31.38	32.39	33.29	34.11	34.86	35.56	36.22	36.89
Δr_{np} (fm)	0.1574	0.1886	0.2103	0.2268	0.2402	0.2514	0.2609	0.2699

TABLE III: Parameters g_ρ and $\Lambda_{\rm v}$ generated from the IUFSU model for different slope L at saturation density n_0 with fixed symmetry energy $E_{\rm sym} = 26.78$ MeV at $n_{\rm fix} = 0.11\,{\rm fm}^{-3}$. The last two lines show the symmetry energy at saturation density, $E_{\rm sym}(n_0)$, and the neutron-skin thickness of ^{208}Pb, Δr_{np}. The original IUFSU model has $L = 47.2$ MeV.

L (MeV)	47.2	50.0	60.0	70.0	80.0	90.0	100.0	110.0
g_ρ	13.5900	12.8202	11.1893	10.3150	9.7537	9.3559	9.0558	8.8192
$\Lambda_{\rm v}$	0.0460	0.0420	0.0305	0.0220	0.0153	0.0098	0.0051	0.0011
$E_{\rm sym}(n_0)$ (MeV)	31.30	31.68	32.89	33.94	34.88	35.74	36.53	37.27
Δr_{np} (fm)	0.1611	0.1739	0.2062	0.2278	0.2441	0.2571	0.2678	0.2770

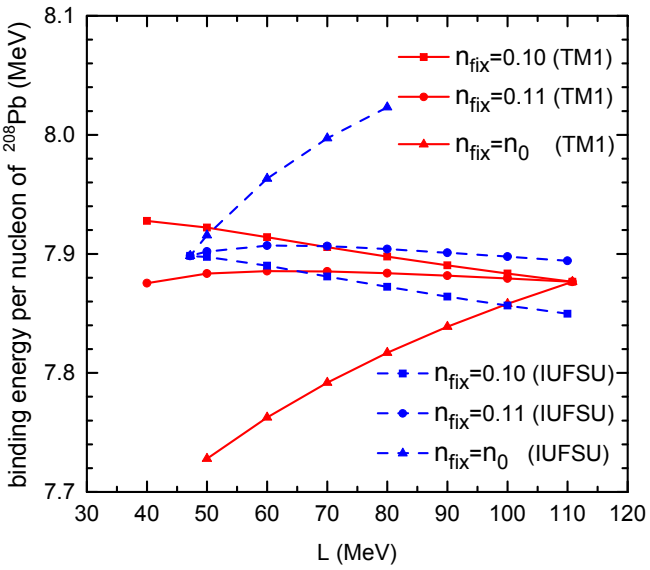

FIG. 1: (Color online) Binding energy per nucleon of ^{208}Pb vs the symmetry energy slope L with different choices of $n_{\rm fix}$ based on the TM1 and IUFSU parametrizations.

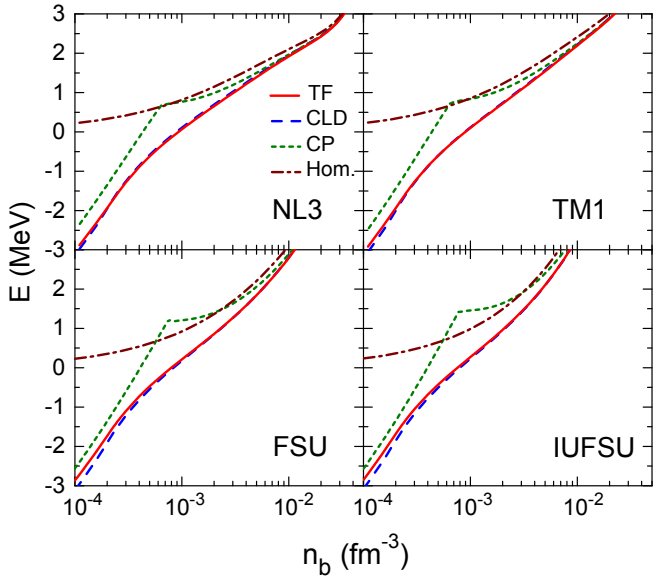

FIG. 2: (Color online) Energy per nucleon, E, as a function of the average baryon density n_b obtained using the TF, CLD, and CP methods with different RMF parametrizations (NL3, TM1, FSU, and IUFSU). For comparison, the results of homogeneous matter (Hom.) are also plotted.

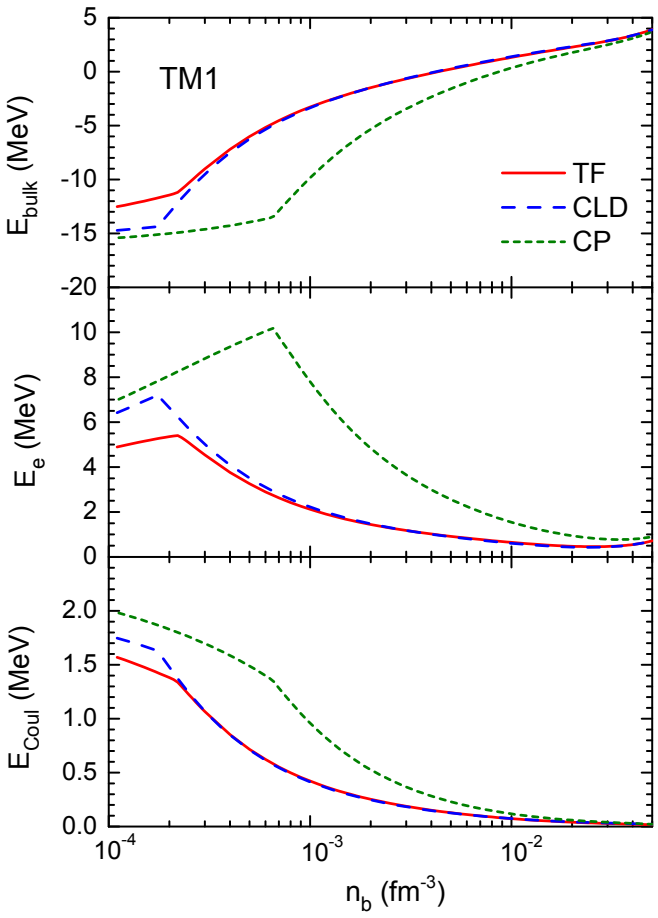

FIG. 3: (Color online) Comparison of the bulk energy per nucleon, $E_{\rm bulk}$ (top panel), the electron kinetic energy per nucleon, E_e (middle panel), and the Coulomb energy per nucleon, $E_{\rm Coul}$ (bottom panel) among the CP, CLD, and TF methods using the TM1 parametrization.

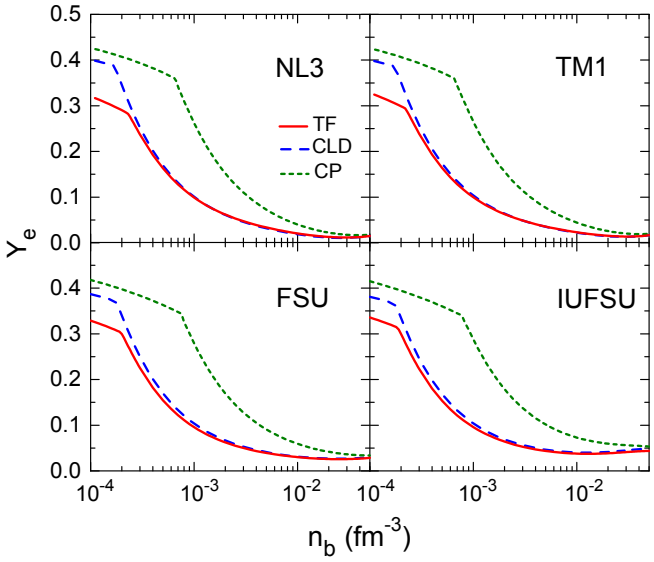

FIG. 4: (Color online) Electron fraction Y_e as a function of n_b obtained using the CP, CLD, and TF methods.

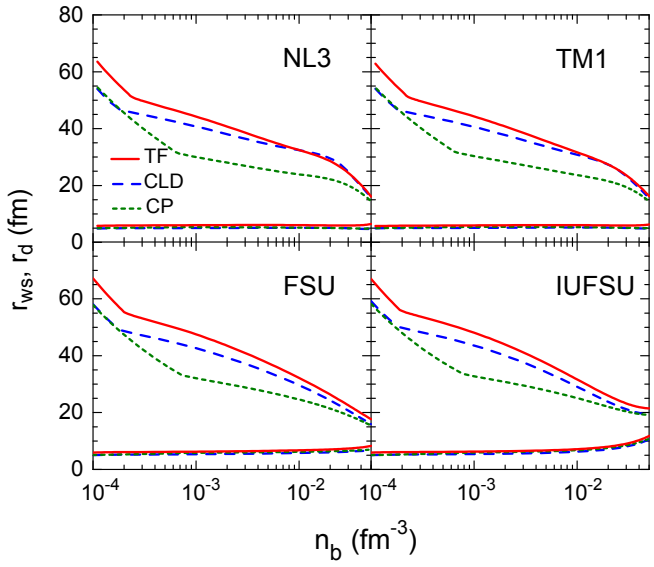

FIG. 5: (Color online) Wigner–Seitz cell radius $r_{\rm ws}$ and droplet radius r_d as a function of n_b obtained using the TF, CLD, and CP methods. r_d in the CP and CLD methods is given in Eq. (21), while it is defined by $r_d = \sqrt{\frac{5}{3}}\langle r_p^2\rangle^{1/2}$ in the TF approximation.

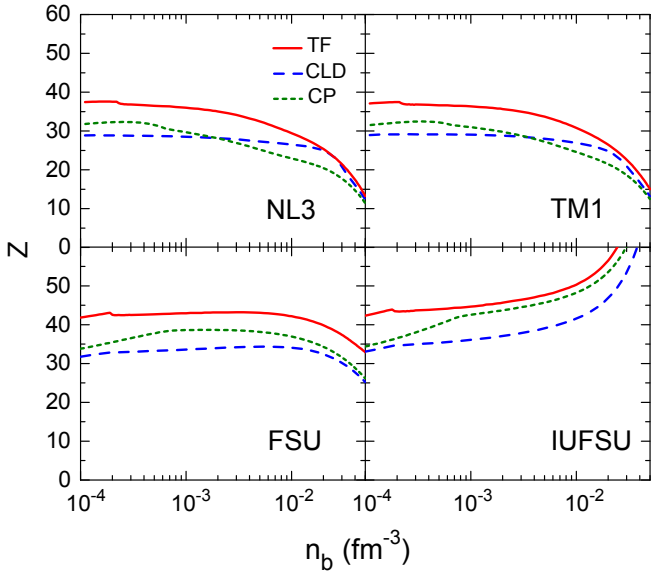

FIG. 6: (Color online) Proton number Z of the droplet as a function of n_b obtained using the TF, CLD, and CP methods.

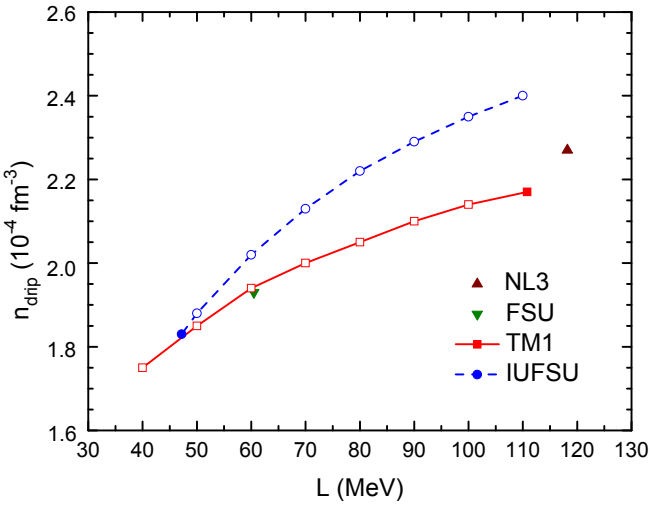

FIG. 7: (Color online) Neutron drip density $n_{\rm drip}$ as a function of L using the two sets of models generated from TM1 (red solid line with squares) and IUFSU (blue dashed line with circles). The results obtained with the original TM1 and IUFSU models are indicated by the filled square and filled circle, respectively. The results of NL3 and FSU are represented by the up and down triangles.

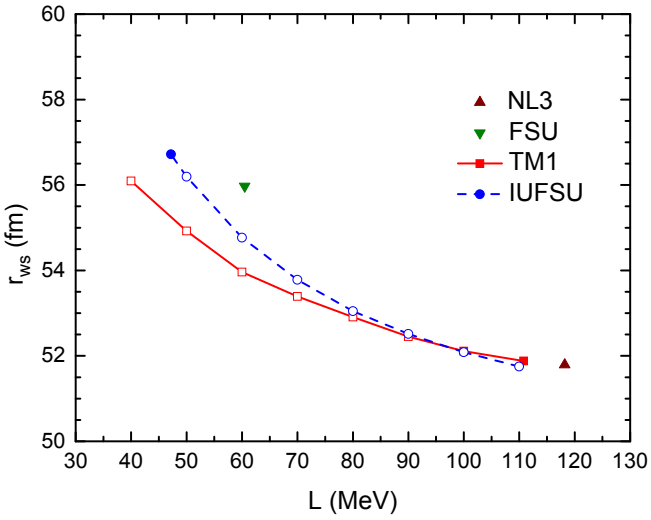

FIG. 8: (Color online) Same as Fig. 7, but for the cell radius $r_{\rm ws}$ at the neutron drip density.

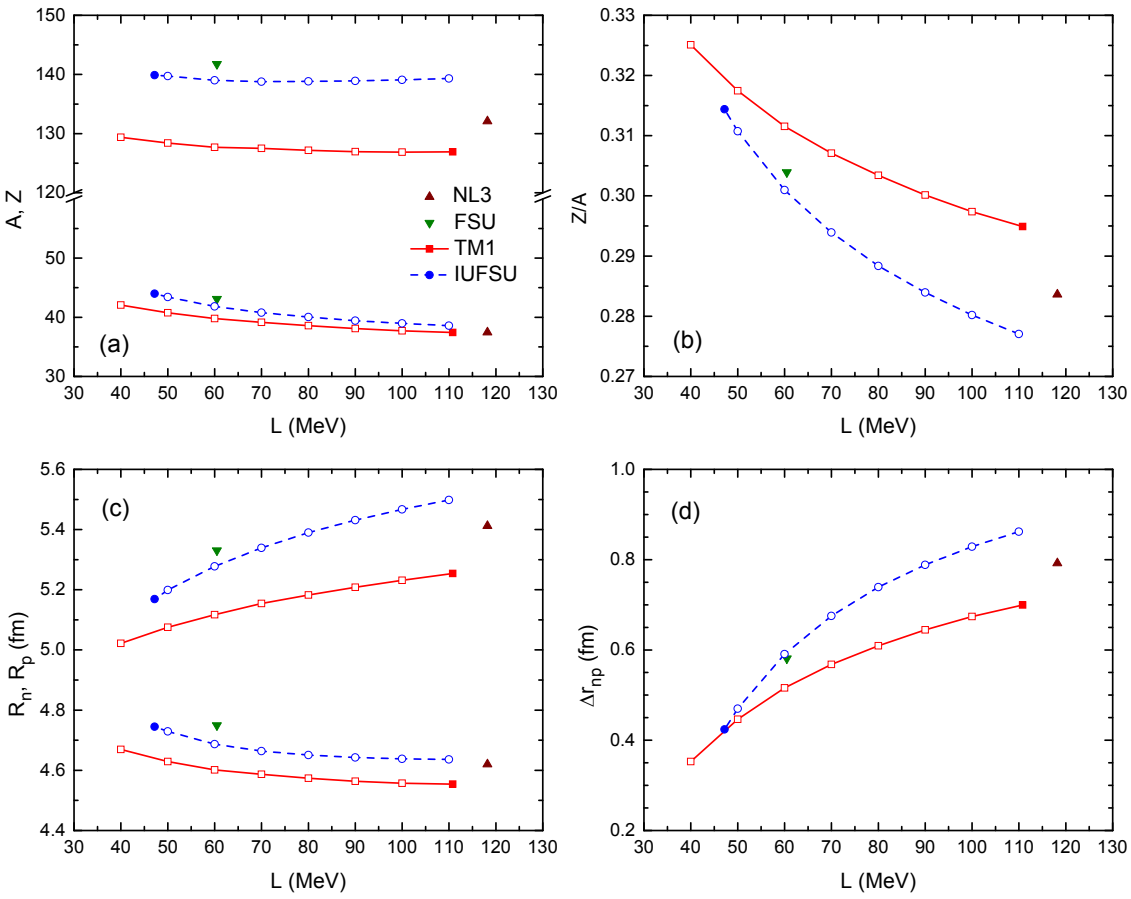

FIG. 9: (Color online) Properties of the nucleus at the neutron drip density vs L obtained in the TF calculation. The nucleon number A and the proton number Z (a), the proton fraction Z/A (b), the rms radius of the neutron R_n and that of the proton R_p (c), and the neutron skin thickness $\Delta r_{np} = R_n - R_p$ (d) are plotted.

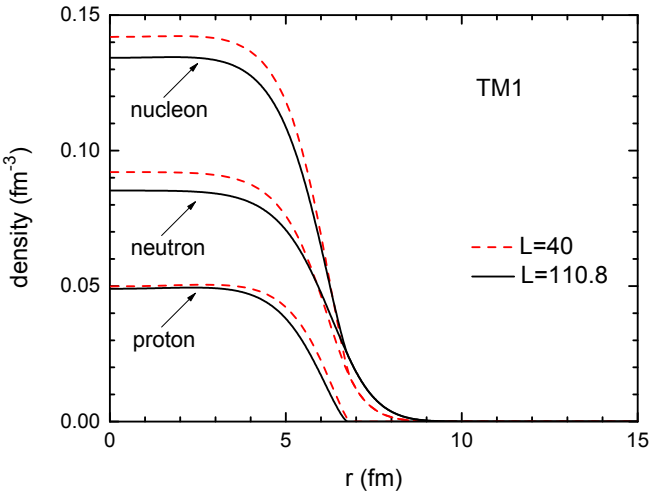

FIG. 10: (Color online) Nucleon density distributions in the Wigner–Seitz cell at the neutron drip density obtained with $L = 110.8$ MeV (black solid lines) and $L = 40$ MeV (red dashed lines) in the set of TM1.

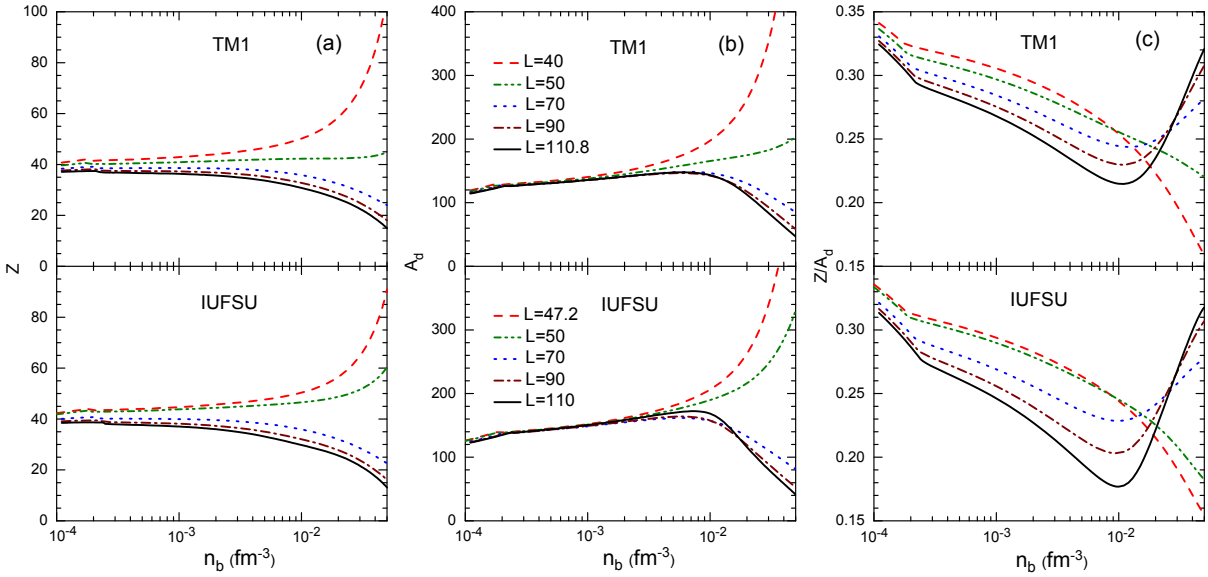

FIG. 11: (Color online) Properties of the nucleus in neutron star crusts, such as the proton number Z (a), the nucleon number A_d (b), and the proton fraction Z/A_d (c), as a function of n_b obtained in the TF approximation using the two sets of generated models.

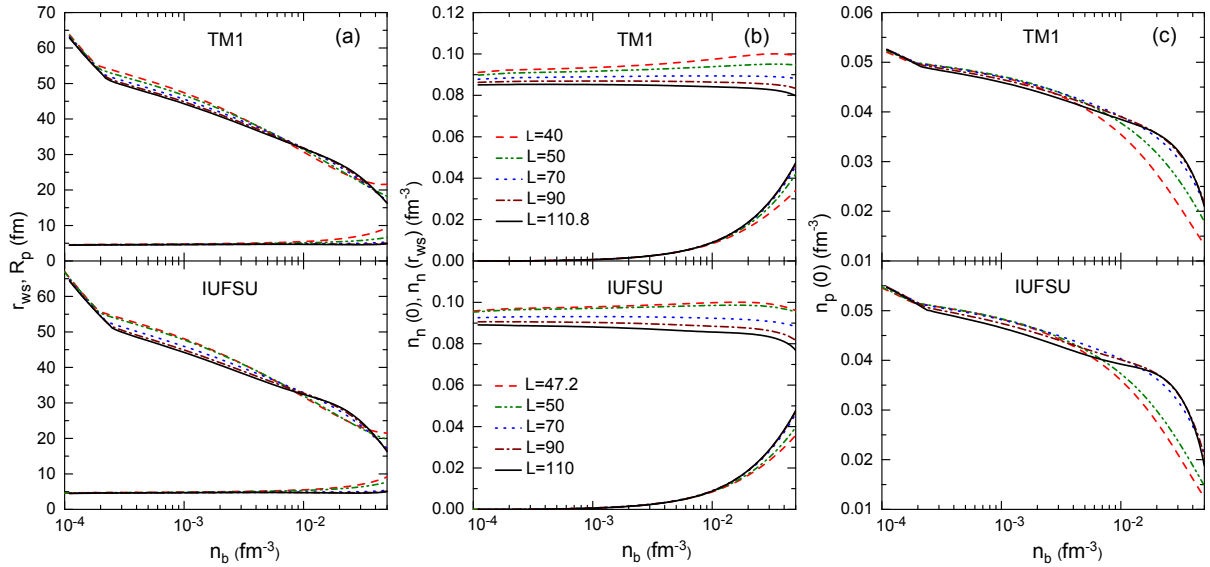

FIG. 12: (Color online) Equilibrium properties of the Wigner–Seitz cell as a function of n_b obtained in the TF approximation using the two sets of generated models. The cell radius $r_{\rm ws}$ and the proton rms radius R_p (a), the neutron density at the center, $n_n(0)$, and that at the boundary, $n_n(r_{\rm ws})$ (b), and the proton density at the center, $n_p(0)$ (c), are plotted.

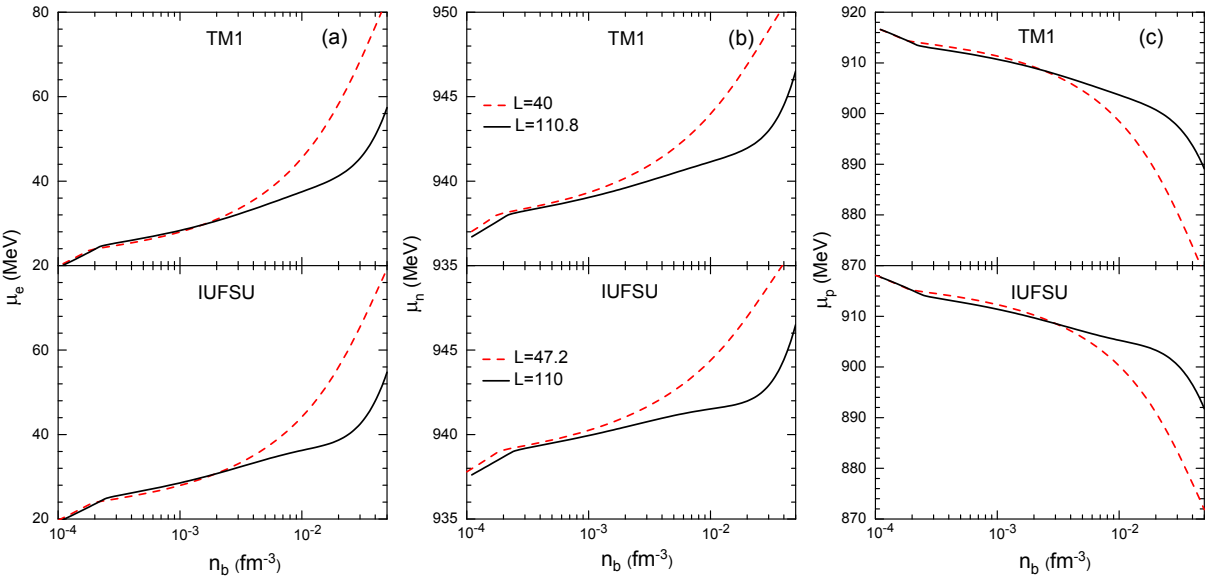

FIG. 13: (Color online) Chemical potentials of electrons, μ_e (a), neutrons, μ_n (b), and protons, μ_p (c), as a function of n_b obtained in the TF approximation with the smallest and largest values of L in the two sets of generated models.

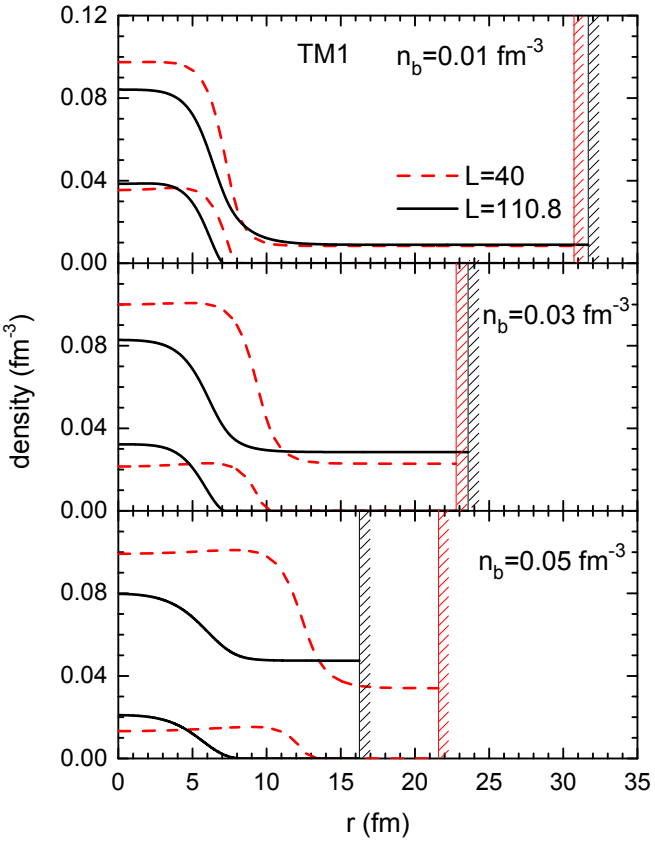

FIG. 14: (Color online) Density distributions of neutrons (upper curves) and protons (lower curves) in the Wigner–Seitz cell at average baryon densities $n_b = 0.01$, 0.03, and $0.05\,\mathrm{fm}^{-3}$ (top to bottom) obtained with $L = 110.8$ MeV (black solid lines) and $L = 40$ MeV (red dashed lines) in the set of TM1. The cell radius r_{ws} is indicated by the hatching.